System Modeling, Characterization, and Design Considerations for Generators in Commercial Watches With Application to Energy Harvesting for Wearables

Tiancheng Xue, Shane Williams, Robert Rantz, Miah Abdul Halim, and Shad Roundy, *Member, IEEE*

***Abstract*—This paper presents the characterization of the energy generators embedded in commercial watches with a focus on the Kinetron microgenerator system. These motion-powered watches are potential benchmarking subjects for any effort to develop wearable energy harvesters, and yet have not been systematically characterized. We have developed a system-level model including both the kinematics of the rotational proof mass and the dynamics of the electromechanical transducer for the energy generator based on a generalized rotational energy harvester model. Our experimental characterization includes both controlled bench-top swing arm tests as well as human subject tests. Multiaxial inertial inputs either constructed or obtained from real-world measurement serve as the inputs in the simulation. These characterization results not only serve as a means for model validation but also to provide insight into the state-of-the-art of commercially available wearable energy harvesting capabilities. The experimentally validated model allows us to perform numerical simulations to study scaling relationships and explore pathways to improved power output.**

***Index Terms*—Characterization, energy harvesting, microgenerators, modeling, wearable devices, watches.**

I. Introduction

ENERGY harvesting for wearable applications has gained significant traction in recent years. It provides a promising alternative to conventional batteries when energy independence is preferred or even necessary. Feasible applications include wearable health monitors and implantable sensors [1]. A major obstacle to harvesting energy in a wearable fashion is the unpredictable nature of the human motion, which is dominated by nonperiodic and low-frequency excitations. A technique coined as frequency up-conversion is often applied in the research communities to efficiently utilize higher frequency resonant harvesters with a low frequency, nonperiodic environmental input [2]–[4]. In the commercial space, however, motion-powered quartz watches have achieved effective frequency up-conversion by different means, often with the involvement of gear trains. In many cases, reported wearable energy harvesting prototypes utilize an eccentrically weighted rotational proof mass [3], [5]–[7] as it can be excited in all directions with no inherent motion limit. The harvesters often resemble the shape of a wrist-worn watch.

Motion-powered quartz watches, sometimes also referred to as automatic quartz, are successful demonstrations of energy harvesting techniques for commercial wearable applications. Examples of these include Seiko Kinetic, Citizen Eco-Drive Duo, and Swatch Autoquartz, which use the microgenerator system (MGS) made by Kinetron as the energy generation unit. Although the latter two have been discontinued, the first is still in production. These motion-powered watches are often overlooked in the wearable energy harvesting literature largely because they are developed empirically (i.e., without the use of predictive modeling) and in the commercial space. Yet they are ideal candidates against which to benchmark for many research endeavors in wearable energy harvesting. Some existing characterization work exists in the literature where the system is often analyzed in isolation without any rotor kinematics or real-world input [8], [9]. Seiko only provides vague descriptions for its power capabilities in the user manual [10], whereas Kinetron claims 600 mJ per day from the MGS [11]. A reasonable estimate of power output is roughly 5 μW on a daily average basis for these watches [12]. An 8 h measurement for the Seiko Kinetic reports a median power of 0.5 μW among subjects [13]. Another full day measurement for the Kinetron MGS reports a total energy generation of 1.1 J [14]. However, for benchmarking purposes, there is a lack of knowledge in terms of power output with respect to specific excitations. In addition, to understand the potential and limitations of these motion-powered watches for wearable energy harvesting better, a thorough model-based characterization is indispensable.

Manuscript received December 5, 2017; revised May 29, 2018; accepted August 7, 2018. Date of publication August 13, 2018; date of current version October 15, 2018. Recommended by Technical Editor L. Zuo. This work was supported by the National Science Foundation (NSF, USA) through the NSF Nanosystems Engineering Research Center for Advanced Self-Powered Systems of Integrated Sensors and Technologies under award number EEC 1160483. *(Corresponding author: Tiancheng Xue.)*

The authors are with the Department of Mechanical Engineering, University of Utah, Salt Lake City, UT 84112 USA (e-mail: tiancheng.xue@utah.edu; u0722038@utah.edu; robert.rantz@utah.edu; halim.miah@utah.edu; shad.roundy@utah.edu).

Color versions of one or more of the figures in this paper are available online at http://ieeexplore.ieee.org.

Digital Object Identifier 10.1109/TMECH.2018.2865307

We have characterized the microgenerator embedded in the Seiko Kinetic watch in a previous work [15] based on a generalized rotational harvester model [16]. The Seiko Kinetic watch employs a sophisticated gear train with a 1:100 ratio to increase the velocity of the rotating magnetic rotor and thus the effective electromechanical coupling, which also ensures an appropriate voltage output for power conditioning. However, this high gear ratio is also reflected on the viscous damping associated with the bearings and reduces the available maximal energy for harvesting [16]. Given the higher damping on the rotational mass that results from the high-ratio gear train, alternative frequency up-conversion techniques might be required to achieve the improved power output that we see in the simulation with reduced mechanical damping [15]. Unlike the Seiko Kinetic, the Kinetron MGS decouples its transducer from the rotational mass with a spring as an intermediate energy storage element. To our knowledge, a full model-based characterization of the Kinetron MGS has never been published in the literature. The characterization includes both bench-top and human subject experiments on power generation, which will shed light on the state-of-the-art in commercial wearable energy harvesting capabilities. In addition, we will study the scaling laws with respect to power output and explore pathways to improved power output in simulation-based studies.

II. Modeling

A. Generalized Rotational Energy Harvester Model

The characterization of the Kinetron MGS is based on the previously developed generalized rotational harvester model [16]. The model predicts an upper bound on energy generation given the six-axis motion inputs and system constraints such as the rotational inertia and the eccentricity of the eccentric proof mass. An electrical and a mechanical rotational viscous damper, namely, b_e and b_m, are applied to the rotational proof mass to represent extracted and lost energy, respectively. This model is an analogy to the linear velocity damped resonant generator model [17], [18], making the assumption that the power dissipated through an optimal viscous damper that represents the electromechanical transducer is the maximum electrical power that can be extracted from the system. This hypothesis has only been proven for linear oscillators under periodic base excitations. For rotational architectures with quasiperiodic or even chaotic excitations such as real-world human motion, we believe a reasonable estimate of the maximum achievable power can be derived based on this assumption nonetheless. In theory, all eccentric-rotor based energy harvesters including both the Seiko Kinetic and the Kinetron MGS should be limited by the predicted upper bound on power output.

The three-dimensional model accounts for five-axis inertial inputs (there is no $\ddot{Z}$) as the harvester can be excited with linear excitations, rotational excitations, or both. As illustrated in Fig. 1, the model can be reduced into two dimensions as the rotation of the eccentric mass is constrained in the *XY*-plane. Applying Newton's second law to this lumped model, we have

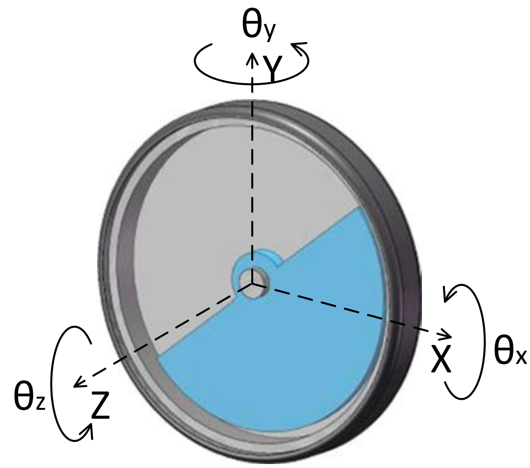

Fig. 1. Generalized eccentric rotor based rotational energy harvester.

$$m\,\ddot{\boldsymbol{r}} = \boldsymbol{F}_h + m\boldsymbol{g} \tag{1}$$

$$I\,\ddot{\psi}_z = -\left(b_m + b_e\right)\dot{\phi}_z + \left(-\boldsymbol{L}\right)\times\boldsymbol{F}_h \tag{2}$$

where the torques are summed at the rotor center of mass. m, I, and $\boldsymbol{L}$ are the mass, the moment of inertia, and the eccentricity vector (its amplitude is denoted L) of the rotor, respectively. $\boldsymbol{F}_h$ and $\boldsymbol{g}$ are the forces from the housing via the supporting shaft and the gravitational acceleration, respectively. $\boldsymbol{r}$ and ψ_z denote the absolute linear and angular displacement of the rotor, whereas ϕ_z denotes its relative angular displacement with respect to the housing. The governing equation of the system [5] is derived as

$$\ddot{\phi}_z = \frac{-\left(b_m + b_e\right)\dot{\phi}_z + mL\left[\left(\ddot{X} - g_x\right)\sin\phi_z - \left(\ddot{Y} - g_y\right)\cos\phi_z\right]}{I + mL^2} - \ddot{\theta}_z \tag{3}$$

where $\ddot{X}$, $\ddot{Y}$, and $\ddot{\theta}_z$ are the linear and rotational acceleration inputs to the system. Conveniently, the combination of the linear accelerations and the negative gravitational accelerations are usually the raw accelerometer output, which can be obtained alongside the rotational velocity from an inertial measurement unit (IMU). The power output for this viscously damped generalized harvester model is determined by

$$P = b_e\,\dot{\phi}_z^2. \tag{4}$$

The full derivation of the model is given in the Appendix.

B. Kinetron MGS Model

As illustrated in Fig. 2 [11], the Kinetron MGS utilizes the oscillating weight to capture the inertial energy from human motion. The bidirectional rotation of the oscillating weight is converted to the unidirectional winding of a spiral spring through a mechanical rectifier, which consists of two ratchet wheels. The rectifier imposes a backlash deadband of approximately

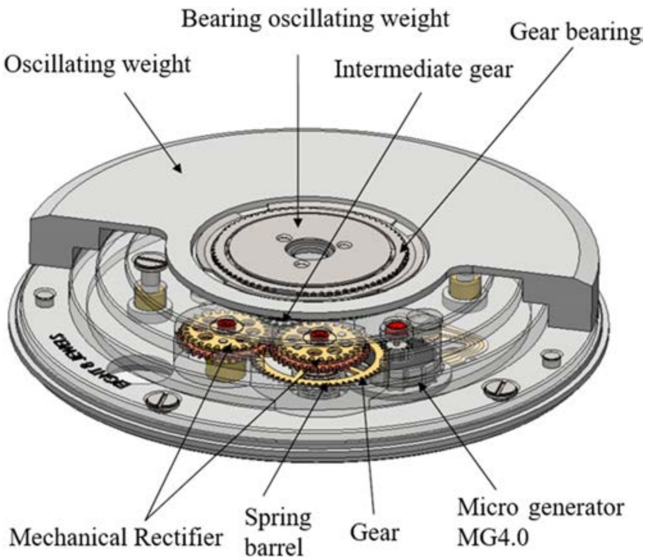

Fig. 2. Components of the Kinetron microgenerator system (MGS).

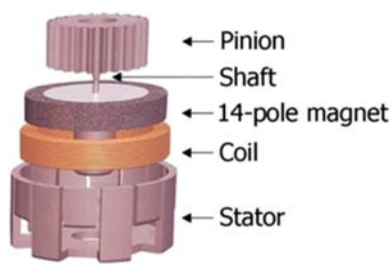

Fig. 3. Components of the microgenerator MG4.0.

10° when the oscillating weight switches direction and a new rectification is initiated. The upper extremity of the spring is tied to the end of the mechanical rectifier and the lower extremity is fastened to a gear that turns the microgenerator at a ratio of 1 to 5. An exploded view of the microgenerator is shown in Fig. 3 [19]. The generator comprises a 14-pole magnet as the generating rotor and a claw-pole stator. As the spring restoring torque builds up, the generating rotor is held by the detent (or cogging) torque induced by the claw structure of the stator until the restoring torque surpasses the maximum detent torque. Then a sudden spring jump occurs and turns the generating rotor at a high speed, which induces changes of magnetic flux through the coil, and thus electricity. The spring functions as an intermediate energy storage element and the generator itself is highly decoupled from the characteristics of the environmental excitation. However, under extreme conditions when the oscillating weight moves sufficiently fast, the spring degenerates to a fixed connection.

The entire MGS can be viewed as an intermittently coupled system between the oscillating weight structure and the microgenerator depending on the state of the mechanical rectifier. Hence, we can initially model two subsystems individually. When the rectifier operates in the deadband and the spring is disengaged, the governing equation for the oscillating weight is identical to (3) with the absence of the electrical damper (i.e., the microgenerator in this case). It will be shown later that a hybrid damping mechanism with a Coulomb damping torque T_c in addition to the viscous damper better represents the frictional energy loss associated with the jewel bearings and the gear transmission, Eqn. (5) shown at the bottom of this page:

$$\ddot{\phi}_z = \frac{-b_m \dot{\phi}_z - T_c \text{sgn}\left(\dot{\phi}_z\right) + mL\left[\left(\ddot{X} - g_x\right)\sin\phi_z - \left(\ddot{Y} - g_y\right)\cos\phi_z\right]}{I + mL^2} - \ddot{\theta}_z \tag{5}$$

On the other hand, when not operating in the deadband, the state of the microgenerator is determined by the summation of the torques applied including the spring restoring torque T_k, the electromagnetic torque T_{em}, the viscous damping torque T_f, and the detent torque T_d:

$$\ddot{\alpha} = \frac{T_k + T_{\text{em}} + T_f + T_d}{I_{\text{gt}}} \tag{6}$$

where I_{gt} is the moment of inertia of the generating rotor (i.e., the 14-pole magnet) and we use α to denote its angular displacement. Accordingly, the flux linkage is determined by the maximum magnetic flux $\Phi_{\max}$ and the phase of the generating rotor:

$$\Phi_f\ (\alpha) = \Phi_{\max}\ \cos(p\alpha)\,. \tag{7}$$

In the equation mentioned above, p denotes the number of pole pairs. The instantaneous electromagnetic torque T_{em} is the product of the armature current i and the derivative of the flux linkage with respect to the generator angle:

$$T_{\text{em}} = i\,\frac{d\Phi_f}{d\alpha} = -\frac{1}{R_c + R_l}\frac{d\Phi_f}{dt}\frac{d\Phi_f}{d\alpha} \tag{8}$$

where R_c and R_l are the resistance of the coil and the load, respectively. Note that for characterization purposes we terminate the coil with a resistive load, whereas in the original MGS system, the voltage output is rectified and stored in a lithium-ion battery. In addition, the inductance of the coil is neglected. The restoring torque of the spiral spring is defined by the difference between the two extremities and the spring stiffness k. In addition, the torque applied to the generator is geared down by a ratio of η_2:

$$T_k = \eta_2\ (\beta - \eta_2\alpha)\,k. \tag{9}$$

Here, we use β to denote the lower extremity angle, which is the output of the mechanical rectifier. When the rectifier overcomes the slippage angle and engages the spring, this lower extremity angle tracks the absolute value of the relative angular displacement of the oscillating weight ϕ_z accumulatively and with a gear up ratio of η_1. We assign b_{gt} as the viscous damping coefficient for the generating rotor, and thus obtain the damping torque as

$$T_f = -b_{\text{gt}}\dot{\alpha}. \tag{10}$$

TABLE I
PARAMETERS FOR THE KINETRON MGS MODEL

Component	Parameter	Value
Oscillating weight	Mass m	4.0×10^{-3} kg
	Moment of inertia about center of mass I	2.6×10^{-7} kg $\cdot$ m^2
	Eccentricity L	6.6×10^{-3} m
Generating rotor	Moment of inertia about center of mass I_{gt}	5.5×10^{-11}kg $\cdot$ m^2
	Number of pole pairs p	7
	Maximum flux linkage Φ_{max}	7.0×10^{-3} V $\cdot$ s
	Maximum detent torque T_D	1.1×10^{-5} N $\cdot$ m
	Coil resistance R_c	3.2×10^2 Ω
Gear train	Oscillating weight to spring ratio η_1	28: 45
	Spring to microgenerator ratio η_2	12: 60

The detent torque is a well-known phenomenon that exists in all claw-pole motors that use permanent magnets. It is the result of a tendency of the rotor to stay in a particular position with respect to the claw of the stator where the permeance of the magnetic circuit is maximized. Although an undesirable byproduct in most applications, the detent torque is indispensable to the functionality of the microgenerator in this case. It allows the spring to accumulate energy and release it at a higher frequency with proper voltage output. In general, electromagnetic generators suffer from low voltage output when the mass velocity is slow. It has been shown that an analytical solution for the detent torque can be derived with the knowledge of the detailed geometry of the stator [20], in the absence of which, however, we can approximate its profile as a sinusoidal function with respect to the phase given that the maximum torque can be experimentally obtained [9]:

$$T_d = -T_D \ \sin\left(2p\alpha\right). \tag{11}$$

Substitute (8)–(11) into (6), we have

$$\ddot{\alpha} = -\frac{\left(b_{\mathrm{gt}} + \frac{p^2\Phi_{\mathrm{max}}^2 \sin^2(p\alpha)}{R_c+R_l}\right)\dot{\alpha} + \eta_2^2 k\alpha + T_D \sin\left(2p\alpha\right) - \beta\eta_2 k}{I_{\mathrm{gt}}}. \tag{12}$$

When the mechanical rectifier operates out of the deadband, the spring is engaged and its restoring torque is reflected on the oscillating weight via the associated gear train. As a result, the governing equation for the oscillating weight structure is modified as, Eqn. (13) shown at the bottom of this page.

Finally, the power output across a resistive load is given by

$$P = R_l \left(\frac{1}{R_c + R_l}\frac{d\Phi_f}{dt}\right)^2. \tag{14}$$

We implement the Kinetron MGS model using (5)–(13) in MATLAB with the parameters listed in Table I [9], [11], [19], [21] and carry out the simulation in the time domain using a numerical ordinary differential equation (ODE) solver. In order to obtain an accurate numerical solution, integrations are restarted at the instances of discontinuity, primarily due to the mechanical rectifier (this is done by two ODE events and a switch-case loop to alternate between (5) and (13) as the governing equation of the oscillating weight based on the state of rectification). The inclusion of Coulomb damping escalates the computational cost at a fixed local error tolerance.

III. DATA COLLECTION

We divided our experimental characterization into two parts: bench-top and human-subject characterization. On one hand, controllable and repeatable bench-top tests provide convenience for model corroboration. On the other hand, on-body tests are essential for any wearable device because they grant insight into the performance and its variation among the population.

A. Bench-Top Data Collection

In the literature, the bench-top characterization of wearable energy harvester prototypes was carried out by conventional linear shaking systems in many cases [3], [22]. Particularly for rotational architectures, a direct rotational input to the rotor itself was sometimes applied, which decouples the energy harvester from the inertial dynamics [7], [9]. We adopted a previously developed driven pendulum test set-up [5], [23] to carry out the bench-top tests for the Kinetron MGS. Driven by a microstepping-enabled stepper motor, the pendulum arm shown in Fig. 4 creates a sinusoidal trajectory at a variety of frequencies (0.8, 0.91, 1.1, and 1.25 Hz) and amplitudes (12.5°, 18°, and 25°). We chose these values to resemble upper limb motion in gait profiles ranging from casual to vigorous walking [23]. This artificial periodic input roughly resembles a human arm in locomotion with the capability to provide rotational excitation in addition to linear accelerations.

The device under test (DUT) was attached at the end of the 50-cm long aluminum arm. The Kinetron MGS was terminated with a resistive load to extract energy from the system. Due to the pulsed nature of the energy generation, we experimentally determine the optimal load by measuring the energy generated per spring jump with a sweep of the resistive load. The optimal load was found to be larger than the coil resistance, which is likely due to the inductive effect and the additional mechanical impedance. However, there was significant inconsistency in terms of power generation per pulse with the same load resistance. This is possibly due to imbalances or asymmetry as a result of manufacturing imperfections. (That is, the maximum detent torque may depend on the resting position of the magnetic rotor.) In addition, the impedance of mechanical components is nonlinear in nature and dependent on the inertial input (including inertial conditions). We have identified a range of

$$\ddot{\phi}_z = \frac{-b_m\dot{\phi}_z - T_c\,\mathrm{sgn}\left(\dot{\phi}_z\right) - \frac{T_k}{\eta_1\eta_2} + mL\left[\left(\ddot{X} - g_x\right)\sin\phi_z - \left(\ddot{Y} - g_y\right)\cos\phi_z\right]}{I + mL^2} - \ddot{\theta}_z \tag{13}$$

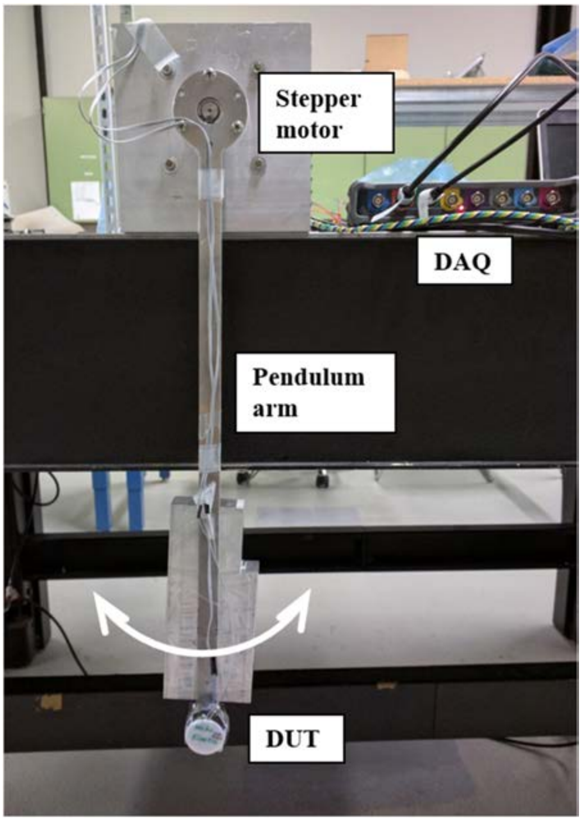

Fig. 4. Photo of the pendulum arm test set-up.

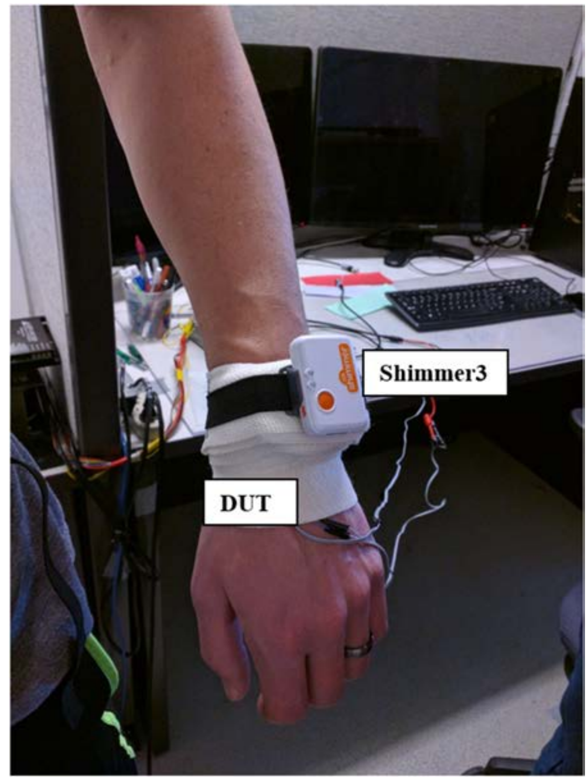

Fig. 5. Photo of the human subject data collection set-up.

load resistance from approximately 500 to 1500 Ω where the energy generation per pulse is nearly optimal. On average, the expectation of power output from a single spring jump is about 90 μJ.

B. Human Subject Data Collection

A total of 30 human subjects including 15 males and 15 females aged between 21 and 45 participated in our data collection. Among the test subjects, 26 are right-handed. A total of six degrees of freedom inertial data from both wrists and the upper arm were recorded using a Shimmer3 IMU made by Shimmer sensing [24] at 50 Hz. These inertial data will serve as the input for model corroboration. As shown in Fig. 5, the IMU was placed directly on the top of the Kinetron MGS, which is wrapped to the subject's wrist with an elastic bandage. Due to this arrangement, the inertial data collected by the IMU are not exactly the same as experienced by the Kinetron MGS. The power output from the MGS across a resistive load was recorded simultaneously using a USB PC oscilloscope made by Pico Technology at 1 MHz to surpass the Nyquist frequency. Test subjects wearing the IMU and the Kinetron MGS were instructed to conduct a series of activities involving upper limb movement including exercising on a treadmill, writing on a whiteboard, and office routines. Details of the tasks are explained in Table II. The choice of a treadmill over simply walking or jogging on the ground is primarily due to its ability to control the velocity for consistency. Although differences exist, the overall gait parameters and kinematic patterns are similar between walking on a treadmill and the ground [25]. However, we have observed a significant variation in the overall motion profile from subject to subject during the data collection process, which manifests as a large variation in energy availability among the population.

TABLE II
REAL-WORLD CHARACTERIZATION TASKS

Tasks		Description
Exercising on a treadmill	Slow walking	Velocity set as 2.5 mph, 2 minutes
	Fast walking	Velocity set as 3.5 mph, 2 minutes
	Jogging	Velocity set as 5.5 mph, 2 minutes
Office routines		Filing documents and serving coffee (repeat with both hands), time varies
Writing on a whiteboard		Writing the text "The quick brown fox jumps over the lazy dog" with the dominant hand, 1 minute

IV. SIMULATION AND EXPERIMENTAL RESULTS

A. Transducer Model Validation

First, we characterize the microgenerator embedded in the Kinetron MGS as a standalone transducer. A no-load simulation of the electromotive force was presented in [9] to reveal its impulsive nature. Yet no experimental validation was provided due to a lack of direct access to the electrical output. In this study, we used MGS samples provided by Kinetron with built-in access to the output from the microgenerator. Fig. 6 illustrates a comparison between simulated and measured voltage output

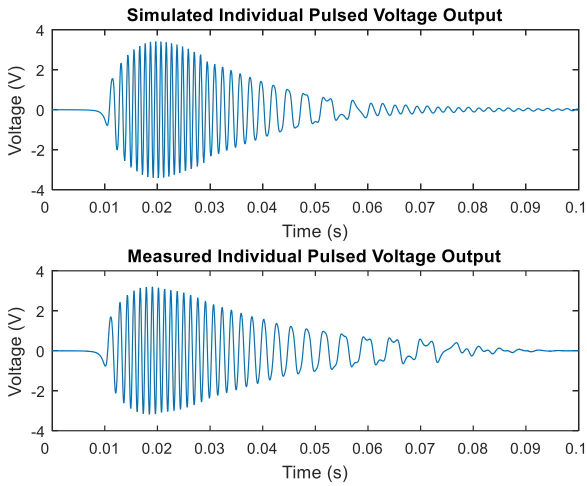

Fig. 6. Simulated and measured individual pulsed voltage output from the Kinetron MGS.

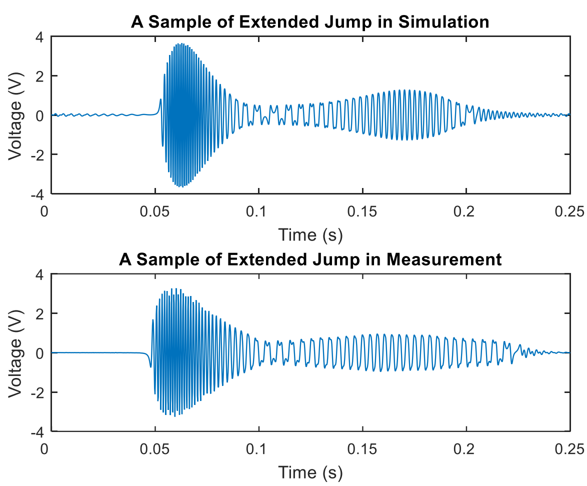

Fig. 7. Samples of extended jump from the Kinetron MGS in simulation and measurement.

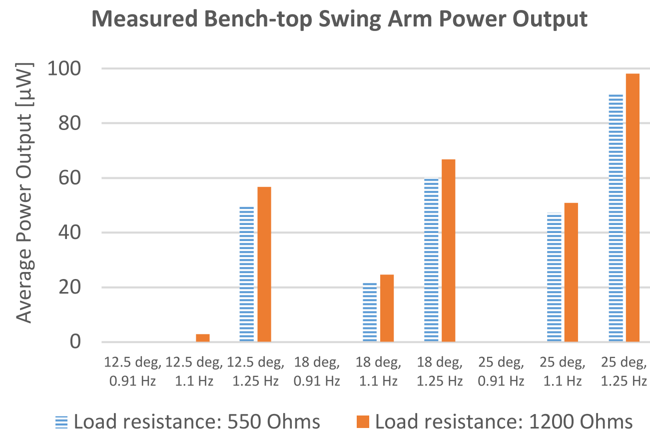

Fig. 8. Measured bench-top swing arm power output from the Kinetron MGS.

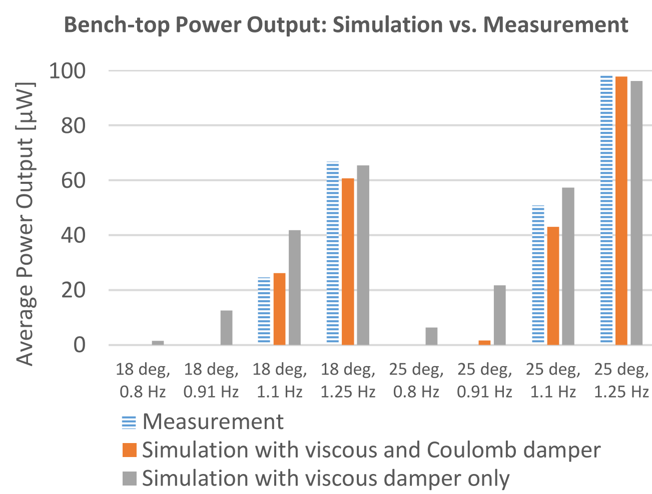

Fig. 9. Simulated and measured bench-top swing arm power output from the Kinetron MGS with a 1200 Ω resistive load.

with a resistive load of 1200 Ω from an individual spring release, which demonstrates good agreement in terms of both frequency and amplitude. However, the viscous damper assumption for the microgenerator model is not able to recreate the nonlinear time-varying damping pattern that exists in the later decay. A closer match is possible with a more complex damping model but it significantly increases the computation cost. This discrepancy can be neglected nonetheless due to the fact that the overall power output is dominated by the initial oscillations.

In addition, the model is able to recreate a phenomenon named extended jump when the oscillating mass moves sufficiently fast that the initial jump is overlaid with a second degenerated jump. Fig. 7 shows examples of this phenomenon in both simulation and measurement that resemble each other.

B. Bench-Top Characterization

We arbitrarily chose two resistance values (550 and 1200 Ω) toward both ends of the optimal range mentioned earlier as the load resistances for characterization. As shown in Fig. 8, a positive correlation exists between the power output and the excitation intensity (i.e., both amplitude and frequency). Each data point is obtained from a 40-s actuation. By our observation, 0.91 Hz exhibits a borderline case in which an individual pulse of energy is only occasionally and inconsistently generated. We denoted those power outputs as zero. Although the power output with the two load resistances is nearly identical, it appears that a 1200 Ω resistor extracts slightly more power. However, this is not a conclusive observation due to the inconsistent initial and the terminal conditions (i.e., the unknown amount of energy stored in the spring). The discrete nature of the power output profile increases the difficulty of eliminating the effect of residual spring energy at weak excitations. Nevertheless, the bench-top swing arm tests provide several data points with good enough repeatability for us to determine the damping parameters for the oscillating weight via trial-and-error data fitting.

Fig. 9 illustrates the parametric fitting result with two damping models for the case with a 1200 Ω resistive load. For the purely viscously damped model, the rotational damping coefficient b_m is 3e – 5 Nm·s, whereas in the hybrid mode, b_m is

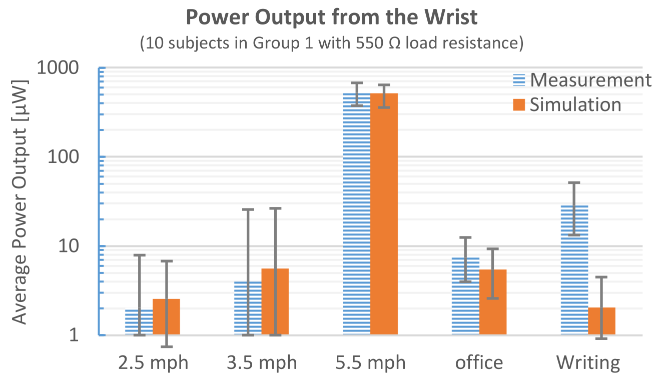

Fig. 10. Measured and simulated power output from the Kinetron MGS on the wrist with a 550 Ω resistive load (group 1).

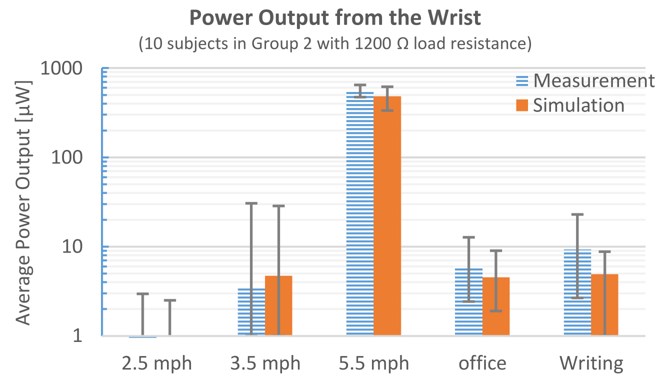

Fig. 12. Measured and simulated power output from the Kinetron MGS on the wrist with a 1200 Ω resistive load (group 2).

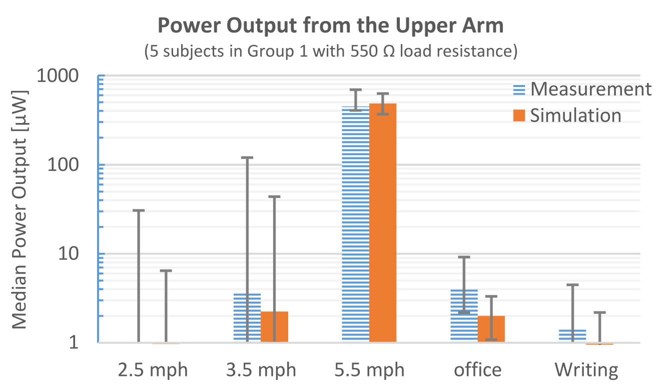

Fig. 11. Measured and simulated power output from the Kinetron MGS on the upper arm with a 550 Ω resistive load (group 1).

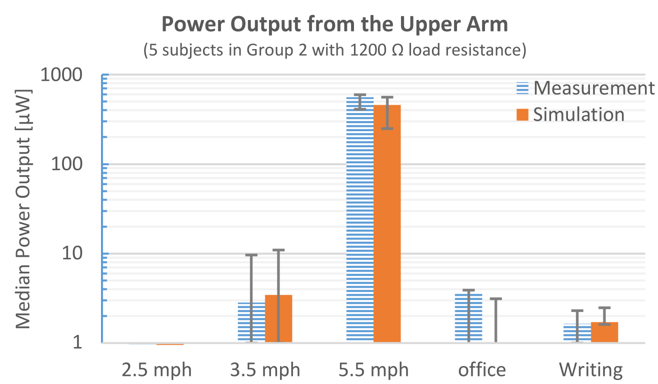

Fig. 13. Measured and simulated power output from the Kinetron MGS on the upper arm with a 1200 Ω resistive load (group 2).

1.5e – 6 Nm·s and the Coulomb torque T_c is 7.5e – 5 Nm. Evidently, the inclusion of a Coulomb damper improves the match by imposing a static torque that prevents the oscillating weight from moving at weak excitations. Thus, the Kinetron MGS produces no power, which is in corroboration of the measured data. The viscous damper only model creates a linear power scaling with no cutoff frequency, which tends to overpredict power output at weak excitations.

C. Human Subject Test Results

Similar to the bench-top test, we divided 30 subjects into 2 groups of 15 to equip with either a 550 or a 1200 Ω load resistance. Among each group, subjects are sorted into three equally numbered subgroups for the devices to be worn on the left wrist, the right wrist, and the upper arm. Figs. 10–13 illustrate all the measured power output along with the simulated results using the corresponding IMU data. For the wrist data with ten subjects, we report the average power output, whereas for the upper arm data with five subjects, we use the median power output due to a more dominant effect of outliers in a smaller sample size. The error bars depict the range of power output among the subjects.

The different resistive loads do not result in significantly different power outputs. (Statistical significance tests indicate that there is no significant difference in power output between tests performed with 550 and 1200 Ω load resistances for 3.5, 5.5 mph, office routing, or writing. *P*-values from *t*-tests range from 0.24 to 0.91.) Jogging at 5.5 mph results in the most consistent power output, whereas other activities especially walking at 2.5 and 3.5 mph result in significant variation. This is in agreement with the large variability in gait pattern, particularly in walking, among subjects from our observation. Some subjects walk with minimal upper limb motion, which generates no power at all. Thus, the average power output could be dominated by a few outliers even though the majority is zero. This is reflected in the IMU data as well. Quantitatively, the amplitude of linear accelerations in $X-$ and Y-direction (raw accelerometer output) at the dominant frequency is, in general, below $2\,\mathrm{m/s^2}$ for walking at both 2.5 and 3.5 mph with a significant variation (extremities are 0.2 and $3\,\mathrm{m/s^2}$). For jogging at 5.5 mph, the acceleration amplitude can go beyond $10\,\mathrm{m/s^2}$. Compared to the wrist, the upper arm location performs equally well in treadmill activities but generates lower power from the office routine and writing on a whiteboard due to a relatively still motion profile, especially in writing. The wrist exhibits a larger range of motion that often goes through a significant change in its orientation with respect to the gravitational field. But, overall both the wrist and the upper arm are promising location candidates for inertial energy extraction to power wearables.

The simulated power output is in good agreement with the measured data in most cases in terms of both the average and

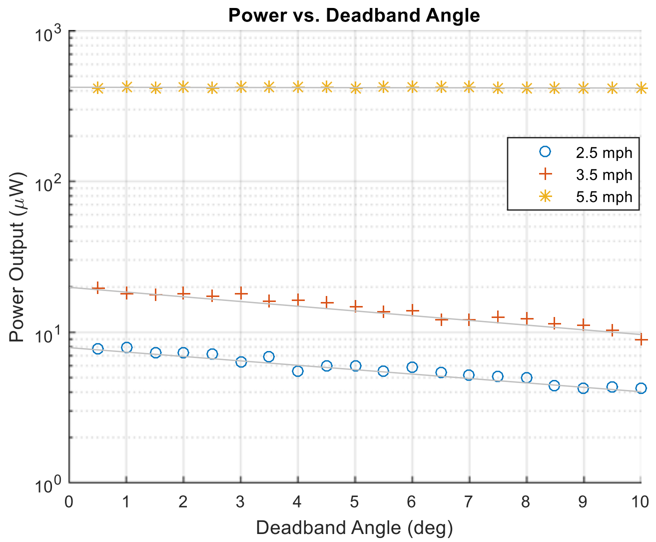

Fig. 14. Simulated power output using sample treadmill inertial data as a function of the mechanical rectifier deadband angle.

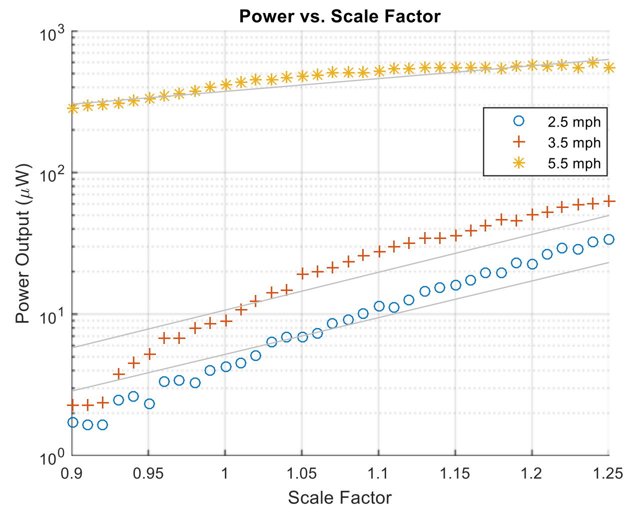

Fig. 15. Simulated power output using sample treadmill inertial data as a function of scale factor.

the variation of power output. However, the predictability deteriorates as the input becomes less energetic and irregular, which resemble the borderline cases in the bench-top swing arm tests. There is some error induced due to the fact that the IMU is placed on the top of the Kinetron MGS, and therefore experiences a slightly different excitation. The elastic bandage could also add to this inaccuracy. In addition, the model itself lacks some accuracy due to the approximated damping parameters obtained from a manual data fitting. The nonlinearity and discontinuity in the model accelerate the error accumulation in the numerical solver as well. Nevertheless, the model appears sufficient to predict power output on an average basis when the effect of initial conditions is eliminated and thus will be used for further investigation.

V. Design Considerations

An overall impression from the human subject test results is that the Kinetron MGS performs relatively well in jogging with approximately 500 μW output on average, whereas in walking it suffers from zero power output from many subjects. What happens in those scenarios is that the device is trapped in the rectification deadband. This is one limiting factor of the design that imposes an excitation threshold for the microgenerator to function. Given how much mild activities occupy in a normal daily routine, this may affect the power capability of the Kinetron MGS for a less energetic population as a wearable energy harvester. To illustrate this, we simulate the power output with hypothetical smaller deadband angles using collected inertial data samples from the wrist. As shown in Fig. 14, there is a trend of increasing power output for walking at both 2.5 and 3.5 mph with decreasing deadband angles. However, it appears that the deadband angle has no apparent effect when the input becomes as vigorous as jogging at 5.5 mph. Under this scenario, the limiting factor becomes the viscous frictional damping due to a higher proof mass velocity. Nevertheless, the elimination of the mechanical rectifier is a potential improvement for the device, which may require an alternative mechanism to engage the spring with the oscillating weight.

The Kinetron MGS was originally designed to be in the shape of a wrist-worn watch. In other applications, with a different form factor or body location, the geometry of the rotor can be altered in the allowed design space to fully capture the available inertial energy. This is another optimization opportunity. In Fig. 15, we use least square regression to illustrate the scaling relationship between the sizing and the power capability with the same inertial inputs used in Fig. 14. We multiply the radius of the oscillating weight by a scale factor while maintaining the same thickness. Note that we keep the same microgenerator parameters for simplicity although there is potential room for optimization with multiple degrees of freedom for a given oscillating weight geometry. In general, a larger design space creates more available power for most activities. The potential improvement appears to be dependent on the excitation as well. Particularly, for walking at 2.5 and 3.5 mph, a 10% increase in radius doubles the power output. Theoretically, more electromechanical coupling can be introduced to further increase the power output when a larger proof mass is available, which can be either implemented in the design of the microgenerator itself or the power conditioning circuitry.

VI. Conclusion

This paper has presented the characterization of the Kinetron MGS, one example of the generators used in motion-powered quartz watches. We derived a system-level model that links the power output directly to the environmental input with a mathematical representation of both the rotor kinematics and the transducer dynamics. We characterized the Kinetron MGS using both repeatable mechanical swing arm tests and human subject tests. The bench-top results are useful for potential benchmarking and model validation. The real-world performance evaluation provides a state-of-art characterization for commercial

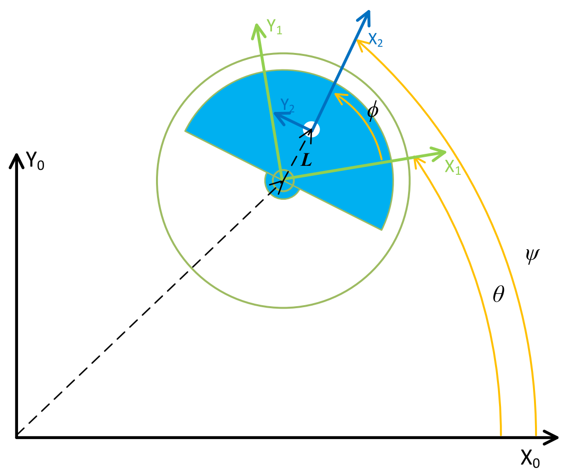

Fig. 16. Schematic of the generalized rotational harvester model in 2D.

wearable energy harvesting capabilities. The model achieves good predictive capability for long-term average power output, especially for vigorous activities.

Through numerical simulations, we found potential improvement with a reduced rectification deadband for less vigorous activities. This, however, may require an alternative design to link the proof mass rotation to the spiral spring. Furthermore, we used the model to evaluate the scaling relationship between the sizing and the power output to investigate the power capabilities for other potential applications. In general, power scales with the rotor radius and the scaling are dependent on the input. In particular, the power output doubles with a 10% increase in the rotor radius for walking at 2.5 and 3.5 mph.

Appendix

In this discussion, the directional subscripts for rotational variables are dropped since the problem is constrained in the local X_1Y_1 plane (see Fig. 16). The absolute acceleration of the rotor can be expressed as

$$\ddot{\boldsymbol{r}} = \boldsymbol{a}_{\text{ref}} + \ddot{\boldsymbol{\theta}} \times \boldsymbol{L} + \dot{\boldsymbol{\theta}} \times \left(\dot{\boldsymbol{\theta}} \times \boldsymbol{L}\right) + 2\dot{\boldsymbol{\theta}} \times \boldsymbol{v}_{\text{rel}} + \boldsymbol{a}_{\text{rel}} \quad \text{(A1)}$$

where $\boldsymbol{a}_{\text{ref}}$ and $\boldsymbol{a}_{\text{rel}}$ are the absolute acceleration of housing, measured from the global inertial frame, and the relative acceleration of the rotor with respect to the housing, respectively. $\boldsymbol{v}_{\text{rel}}$ is the relative velocity of the rotor with respect to the housing. All the vectors in (A1) can be expressed with the Cartesian components along X_1, Y_1, and Z_1 axes as

$$\ddot{\boldsymbol{\theta}} \times \boldsymbol{L} = \ddot{\theta}\, \boldsymbol{k}_1 \times L\left(\cos\phi \boldsymbol{i}_1 + \sin\phi \boldsymbol{j}_1\right) \quad \text{(A2)}$$

$$\dot{\boldsymbol{\theta}} \times \left(\dot{\boldsymbol{\theta}} \times \boldsymbol{L}\right) = \dot{\theta}\, \boldsymbol{k}_1 \times \left(\dot{\theta}\boldsymbol{k}_1 \times L\left(\cos\phi \boldsymbol{i}_1 + \sin\phi \boldsymbol{j}_1\right)\right) \quad \text{(A3)}$$

$$2\dot{\boldsymbol{\theta}} \times \boldsymbol{v}_{\text{rel}} = 2\dot{\theta}\boldsymbol{k}_1 \times L\dot{\phi}\left(-\sin\phi \boldsymbol{i}_1 + \cos\phi \boldsymbol{j}_1\right) \quad \text{(A4)}$$

$$\boldsymbol{a}_{\text{rel}} = \left(-L\dot{\phi}^2\cos\phi - L\ddot{\phi}\sin\phi\right)\, \boldsymbol{i}_1 + \left(-L\dot{\phi}^2\sin\phi + L\ddot{\phi}\cos\phi\right)\boldsymbol{j}_1. \quad \text{(A5)}$$

In addition, acceleration of the housing can be expressed along X_1 and Y_1 axes, which corresponds to the linear acceleration measured by the accelerometer if it is attached to the housing

$$\boldsymbol{a}_{\text{ref}} = \ddot{X}\, \boldsymbol{i}_1 + \ddot{Y}\boldsymbol{j}_1. \quad \text{(A6)}$$

Substitute (A2)–(A6) into (A1)

$$\ddot{\boldsymbol{r}} = \left(\ddot{X} - L\ddot{\psi}\sin\phi - L\dot{\psi}^2\cos\phi\right)\, \boldsymbol{i}_1 + \left(\ddot{Y} - L\ddot{\psi}\cos\phi - L\dot{\psi}^2\sin\phi\right)\boldsymbol{j}_1. \quad \text{(A7)}$$

Similarly, the gravity vector can also be expressed along X_1 and Y_1 axes as

$$\boldsymbol{g} = g_x\, \boldsymbol{i}_1 + g_y\boldsymbol{j}_1. \quad \text{(A8)}$$

The change of gravitational acceleration is a result of the rotational inputs to the system including those in x and y directions.

The governing equation (3) can, therefore, be obtained by substituting (A7) and (A8) into (1) and (2).

Acknowledgment

The authors thank Kinetron for generously supplying hardware and providing assistance in modeling and characterization.

References

[1] V. Misra *et al.*, "Flexible technologies for self-powered wearable health and environmental sensing," *Proc. IEEE*, vol. 103, no. 4, pp. 665–681, Apr. 2015.

[2] T. Galchev, E. E. Aktakka, and K. Najafi, "A piezoelectric parametric frequency increased generator for harvesting low-frequency vibrations," *J. Microelectromech. Syst.*, vol. 21, no. 6, pp. 1311–1320, 2012.

[3] P. Pillatsch, E. M. Yeatman, and A. S. Holmes, "A piezoelectric frequency up-converting energy harvester with rotating proof mass for human body applications," *Sens. Actuators A, Phys.*, vol. 206, pp. 178–185, 2014.

[4] T. Xue and S. Roundy, "On magnetic plucking configurations for frequency up-converting mechanical energy harvesters," *Sens. Actuators A, Phys.*, vol. 253, pp. 101–111, 2017.

[5] T. Xue, H. G. H. G. Yeo, S. Trolier-McKinstry, and S. Roundy, "A wrist-worn rotational energy harvester utilizing magnetically plucked {001} oriented bimorph PZT thin-film beams," in *Proc. 19th Int. Conf. Solid-State Sens., Actuators Microsyst.*, 2017, pp. 375–378.

[6] M. A. Halim, R. Rantz, Q. Zhang, L. Gu, K. Yang, and S. Roundy, "Electromagnetic energy harvesting from swing-arm motion using rotational eccentric mass structure," in *Proc. 19th Int. Conf. Solid-State Sens., Actuators Microsyst.*, 2017, pp. 1863–1866.

[7] J. Nakano, K. Komori, Y. Hattori, and Y. Suzuki, "MEMS rotational electret energy harvester for human motion," *J. Phys. Conf. Ser.*, vol. 660, 2015, Art. no. 12052.

[8] J. Wang, W. Wang, G. W. Jewell, and D. Howe, "Design of a miniature permanent-magnet generator and energy storage system," *IEEE Trans. Ind. Electron.*, vol. 52, no. 5, pp. 1383–1390, Oct. 2005.

[9] M. Lossec, B. Multon, H. Ben Ahmed, and H. Ben Ahmed, "Micro-kinetic generator: Modeling, energy conversion optimization and design considerations," in *Proc. 15th IEEE Mediterranean Electrotech. Conf.*, 2010, pp. 1516–1521.

[10] Seiko Corp., "Parts catalogue/technical guide cal. 5M62A, 5M63A."

[11] Kinetron, "Micro generator system '26.4'," 2014. [Online]. Available: http://www.kinetron.eu/wp-content/uploads/2015/01/MGS-26.4.pdf. Accessed on: Sep. 01, 2017.

[12] P. D. Mitcheson, E. M. Yeatman, G. K. Rao, A. S. Holmes, and T. C. Green, "Energy harvesting from human and machine motion for wireless electronic devices," *Proc. IEEE*, vol. 96, no. 9, pp. 1457–1486, Sep. 2008.

[13] G. Görge, M. Kirstein, and R. Erbel, "Microgenerators for energy autarkic pacemakers and defibrillators: Fact or fiction?" *Herz*, vol. 26, no. 1, pp. 64–68, 2001.

[14] M. Magno, L. Spadaro, J. Singh, and L. Benini, "Kinetic energy harvesting: Toward autonomous wearable sensing for Internet of Things," in *Proc. Int. Symp. Power Electron. Electr. Drives, Automat. Motion*, 2016, pp. 248–254.

[15] T. Xue, S. Kakkar, Q. Lin, and S. Roundy, "Characterization of micro-generators embedded in commercial-off- the-shelf watches for wearable energy harvesting," *SPIE Smart Struct. Mater. Nondestruct. Eval. Health Monit. Int. Soc. Opt. Photon.*, vol. 9801, pp. 1–8, 2016.

[16] T. Xue, X. Ma, C. Rahn, and S. Roundy, "Analysis of upper bound power output for a wrist-worn rotational energy harvester from real-world measured inputs," *J. Phys. Conf. Ser.*, vol. 557, no. 1, pp. 3–7, 2014.

[17] P. D. Mitcheson, T. C. Green, E. M. Yeatman, and A. S. Holmes, "Architectures for vibration-driven micropower generators," *J. Microelectromech. Syst.*, vol. 13, no. 3, pp. 1–12, 2004.

[18] E. Halvorsen, C. P. Le, P. D. Mitcheson, and E. M. Yeatman, "Architecture-independent power bound for vibration energy harvesters," *J. Phys. Conf. Ser.*, vol. 476, pp. 117–121, 2013.

[19] Kinetron, "The 14-pole micro generator with Sm_2Co_{17} magnet (MG4.0)," 2014. [Online]. Available: http://www.kinetron.eu/wp-content/uploads/2014/04/MG4.0.pdf. Accessed on: Sep. 01, 2017.

[20] D. Zarko, D. Ban, and T. A. Lipo, "Analytical solution for cogging torque in surface permanent-magnet motors using conformal mapping," *IEEE Trans. Magn.*, vol. 44, no. 1, pp. 52–65, Jan. 2008.

[21] Kinetron, "The micro generating system for a watch," 2014. [Online]. Available: http://www.kinetron.eu/wp-content/uploads/2014/04/MGSWatch.pdf. Accessed on: Sep. 01, 2017.

[22] Y. Naruse, N. Matsubara, K. Mabuchi, M. Izumi, and S. Suzuki, "Electrostatic micro power generation from low-frequency vibration such as human motion," *J. Micromech. Microeng.*, vol. 19, no. 9, 2009, Art. no. 94002.

[23] R. Rantz, T. Xue, Q. Zhang, L. Gu, K. Yang, and S. Roundy, "Comparative analysis of wrist-worn energy harvesting architectures," *J. Phys. Conf. Ser.*, vol. 773, no. 1, pp. 10–13, 2016.

[24] "IMU sensor development kit | wireless IMU sensor | 9DOF motion sensor | IMU development kit." [Online]. Available: http://www.shimmersensing.com/products/shimmer3-development-kit. Accessed on: Nov. 08, 2017.

[25] S. J. Lee and J. Hidler, "Biomechanics of overground vs. treadmill walking in healthy individuals," *J. Appl. Physiol.*, vol. 104, no. 3, pp. 747–55, Mar. 2008.

Tiancheng Xue received the B.Eng. degree in mechanical engineering from the Huazhong University of Science and Technology, Wuhan, China, in 2013. He is currently working toward the Ph.D. degree at the Integrated Self-Powered Sensing Lab, Department of Mechanical Engineering, University of Utah, Salt Lake City, UT, USA.

His research interest focuses on inertial energy harvesting from human motion.

Shane Williams is currently working toward the B.S. degree in mechanical engineering at the University of Utah, Salt Lake City, UT, USA.

He was an Undergraduate Research Assistant with the Integrated Self-Powered Sensing Lab and currently works with Grip6.

Robert Rantz received the B.S. degree in mechanical engineering from Florida State University, Tallahassee, FL, USA, in 2012. After two years of working in product development, he resumed his studies at the University of Utah, Salt Lake City, UT, USA, where he is currently working toward the Ph.D. degree.

His research at the Integrated Self-Powered Sensing Lab focuses on dynamical structures in vibration energy harvesting.

Miah Abdul Halim received the Ph.D. degree in electronic engineering from Kwangwoon University, Seoul, South Korea, in 2016.

He worked toward the Ph.D. degree in wideband vibration energy harvesting from low-frequency vibration as well as human-body-induced motion. Prior to his Ph.D. study, he worked as a Lecturer with the Faculty of Engineering, Prime University, Dhaka, Bangladesh. He is currently working as a Postdoctoral Research Associate with the Department of Mechanical Engineering, University of Utah, Salt Lake City, UT, USA. He is working on energy harvesting for wearable smart devices applications. He has more than 40 publications in peer-reviewed journals and reputed international conferences, and holds 2 patents. His main research interests include micro-electromechanical systems, self-powered wearables, body area networks for health Internet of Things, and high-frequency ultrasound for biomedical imaging.

Dr. Halim has also served as a reviewer for various prestigious peer-reviewed journals, a Technical Program Committee Member of international conferences, and a Lead Guest Editor of a special issue in *Shock and Vibration*.

Shad Roundy (M'13) received the M.S. and Ph.D. degrees in mechanical engineering from the University of California, Berkeley, Berkeley, CA, USA in 2000 and 2003, respectively.

He joined the faculty at the University of Utah in 2012 where he is currently an Associate Professor in the Department of Mechanical Engineering. From 2005 to 2012 he worked in the MEMS industry developing tire pressure sensors, accelerometers, gyroscopes, and energy harvesters. From 2003 to 2005 he was a Lecturer at the Australian National University. His research interests include energy harvesting, wireless power transfer, and more generally MEMS sensors and actuators.